Torque Distribution-Based Range Extension Control System for Longitudinal Motion of Electric Vehicles by LTI Modeling With Generalized Frequency Variable

Yafei Wang, Hiroshi Fujimoto, *Senior Member, IEEE*, and Shinji Hara, *Fellow, IEEE*

***Abstract*—Electric vehicles (EVs) have been identified as alternatives to traditional engine vehicles because they have no tailpipe emissions and are cheaper to operate. However, limited mileage per charge partially prevents EVs from becoming popular. Although high-efficiency motors and large batteries can be employed to increase the cruising range per charge, pure control approaches for energy saving are more promising. To increase the cruising range of EVs equipped with front and rear in-wheel-motors, this paper proposes an optimal torque distribution algorithm for longitudinal motion by considering the transfer of weight between front and rear axles and motor losses. Then, by modeling an EV as a linear time-invariant (LTI) system with generalized frequency variables, a distributed control concept is proposed, in which part of the main controller's task is allocated to the local controllers. A stability criterion is established for the controller design, and the effectiveness of the proposed range extension control system is verified by both simulations and experiments.**

***Index Terms*—Electric vehicle (EV), energy management system, generalized frequency variable, linear time-invariant (LTI) modeling, torque distribution.**

NOMENCLATURE

μ_i	Friction coefficient between the ith wheel and road.
λ_i	Slip ratio of ith wheel.
ω_i	ith wheel's angular velocity.
$\omega_{e,i}$	Electrical angular velocity of the ith motor.
ρ_{air}	Air density.
a_x	Longitudinal acceleration rate
f_R	Rolling resistance coefficient.
g	Gravitational acceleration.
h_{aero}	Height at which equivalent aerodynamic force acts.
$i_{cd,i}$	d-axis iron loss current of the ith motor.
$i_{cq,i}$	q-axis iron loss current of the ith motor.
$i_{d,i}$	d-axis current of the ith motor.
$i_{q,i}$	q-axis current of the ith motor.
k	Front-rear torque distribution ratio.
k_{opt}	Optimal torque distribution ratio
l	Distance from front wheel to rear wheel.
l_d	Travel distance of the speed pattern
$D_{s,i}$	Driving stiffness of the ith wheel.
F_{aero}	Air resistance.
F_{all}	Total driving force.
F_i	Driving force of the ith wheel.
F_{roll}	Rolling resistance.
$K_{t,i}$	Torque coefficient of the ith motor.
$M_{\mathrm{roll},i}$	Rolling resistance moment of the ith wheel.
P_{copper}	Total copper loss
$P_{c,i}$	Copper loss of the ith motor.
P_f	Friction loss.
$P_{i,i}$	Iron loss of the ith motor.
P_{iron}	Total iron loss.
P_{in}	Input power to the inverters.
P_{inv}	Total inverter loss.
P_{out}	Output power of the motors.
$R_{a,i}$	Armature winding resistance of the ith motor.
$R_{c,i}$	Equivalent iron loss resistance of the ith motor.
N_i	Normal force of the ith wheel.
T_i	Driving torque applied to the ith wheel.
$V_{\omega,i}$	Velocity of the ith wheel.
V_x	Vehicle velocity.

Manuscript received March 6, 2014; revised January 12, 2015, March 24, 2015, March 31, 2015, and April 17, 2015; accepted April 28, 2015. Date of publication June 11, 2015; date of current version February 12, 2016. Recommended by Technical Editor Y. Li.

Y. Wang and H. Fujimoto are with the Department of Advanced Energy, Graduate School of Frontier Sciences, The University of Tokyo, Chiba 277-8561, Japan (e-mail: wang@hori.k.u-tokyo.ac.jp; fujimoto@k.u-tokyo.ac.jp).

S. Hara is with the Department of Information Physics and Computing, Graduate School of Information Science and Technology, The University of Tokyo, Tokyo, 113-8656, Japan (e-mail: Shinji_Hara@ipc.i.u-tokyo.ac.jp).

Color versions of one or more of the figures in this paper are available online at http://ieeexplore.ieee.org.

Digital Object Identifier 10.1109/TMECH.2015.2444651

I. INTRODUCTION

ELECTRIC vehicles (EVs) have been gaining attention from both industry and academic fields as green solutions for future transportation. However, limited cruising range per charge prevents EVs from receiving public recognition [1] to a certain extent. A straightforward solution to this issue is to increase battery size, but cost and limited onboard space render it impractical in many cases. Other methods that focus on developing additional charging infrastructure, such as charging station planning [2] and wireless charging while driving [1] have been studied. Some energy harvesting devices for energy efficiency improvement have been described [3], e.g., onboard shock absorbers that can harvest vertical vibration energy. Along with developing motors, the operating range of EVs can be increased

by utilizing energy more efficiently [4]. These approaches rely on additional facilities or onboard hardware; meanwhile, energy control algorithms for EVs with a distributed drive structure have only been studied in recent years. A review paper [5] categorized these studies into two: the longitudinal motion case and the lateral motion case. For lateral motion, lateral stability has to be addressed along with the energy conservation, which was done by one of the authors' former team in [6]. This study focuses on longitudinal motion, which is a complement to the lateral case of the range extension control system (RECS). In a recent study for energy management in longitudinal motion, a torque distribution strategy was investigated for a front-and-rear-wheel-driven EV by considering iron and copper losses of motors. Its effectiveness was demonstrated using a standard driving cycle on a test bench [7]. In another project, a cost function strategy for energy consumption was designed using particle swarm optimization, and this method was proven to be effective in a hardware-in-the-loop system [8]. A load transferring and slip ratio control method during acceleration and braking had been studied for front-rear-independently driven EVs [9]. This strategy optimizes the distribution ratio of driving/braking torques on front and rear wheels, and energy consumption was shown to be reduced. An EV with four brushless dc in-wheel motors (IWMs) was studied, and torque distribution algorithms that can minimize consumed power for the longitudinal motion of EVs were investigated using a trapezoid speed pattern [10], [11]. In our research, an EV with four in-wheel-type permanent magnet synchronous motors (PMSMs) was considered, and the input power to the motor controllers (inverters) was modeled as a convex function of k, which can be optimized to minimize the required power for the longitudinal motion of EVs.

On the other hand, an increasing number of control functions related to safety, comfort, and efficiency are desired for advanced performances of EVs [12], [13]. If all of these functions were implemented in a central processor, the complexity and processing load would increase considerably. Moreover, an EV with two pairs of IWMs is an overactuated system, and the allocation of control inputs for objectives, such as cruising range extension, has to be considered. To address these two issues, a control allocation-based distributed control approach can be employed. A main-loop–servo-loop structure was proposed for vehicle dynamics control, where the main loop calculates desired forces and yaw moment and the servo loop computes the optimal control input for each actuator [14]. Another work proposed a three-level control strategy to achieve optimal torque distribution for four IWMs, where the first level generates desired yaw moment, the second level distributes the desired longitudinal tire forces, and the third level controls slip ratio of the wheels [15]. Three energy-efficient control allocation schemes were proposed and compared for longitudinal speed tracking control of an electric ground vehicle (EGV) with four IWMs [10], and both simulated and experimental results indicated reduced power consumption by applying the proposed algorithms. For speed pattern generation of longitudinal motion, another paper proposed a method to compute the front-and-rear-forces for an all-wheel drive vehicle that moves along a specified path [16], and the method was demonstrated for a vehicle moving at optimal speeds over a bump. However, most research on control allocation did not provide a generalized stability guarantee for the overall system and some of them only provide a stability criterion for the inner loop [17].

Proposed by Hara *et al.*, a formation control methodology was investigated for distributed homogeneous dynamic agents that are locally stabilized by identical controllers [18]–[20]. Considering that the stability of the overall system cannot be guaranteed even if all of the local systems are stable, a stability criterion for linear systems with generalized frequency variables was established. Specifically, a large scale system denoted by $L(s)$ is assumed, the transfer function's "s" variable is replaced with a rational function "$\phi\ (s)$," and $G(s)$ is defined as $L(\phi(s))$. Then, the Lyapunov stability of multiagent coordination is transformed into one observing the relationship between the pole locations of $L(s)$ and the region of $\phi(s)$ in the complex plane. Based on this concept, the four IWMs of an EV are treated as four local systems in this study, and each of them is controlled by an inverter, i.e., an IWM and an inverter formulate an agent. The central controller (vehicle main controller) allocates driving torque to the four agents to extend cruising range, by considering motor losses and weight transfer between the front and rear axles. The contributions of this paper are twofold. First, an EV with four IWMs was modeled as a linear time-invariant (LTI) system with four generalized frequency variables. Therefore, the stability of the control system can, therefore, be analyzed by simply checking the pole locations of the global system and the region of local dynamics in the complex plane. In fact, this proposed modeling provides a framework for stability analysis of control allocation problems for EVs with two pairs of IWMs, which has rarely been explored in the existing literature. Second, in consideration of the vehicle speed, the output power of the motors was modeled as a convex function of k. Moreover, based on the PMSM's equivalent circuit, copper and iron losses can be also modeled as convex functions of k. Therefore, k can be optimally calculated to minimize the sum of motor output power and losses, i.e., the driving torque can be optimally distributed between the front-rear axles for efficiency, which provides an added value for front-rear-independent-drive EVs.

II. System Description and Modeling

An EV with four IWMs can be seen as a control system with four agents: the vehicle controller works as a central coordinator, and the four wheels are controlled by local inverters. The global-local structure is illustrated in Fig. 1, where the global coordinator calculates required torques, and then, sends commands to the inverters to control the four IWMs.

A. Vehicle and Wheel Dynamics

To propel the EV, the total driven force of the IWMs has to overcome the forces caused by wind resistance, rolling resistance, and inertial effects. Fig. 2 shows the force analysis of an EV with four driving IWMs, and the equation to describe this model can be given as (1), in which F_{aero} and F_{roll} were neglected in the controller design. However, these two terms were considered in the plant model for the simulations in

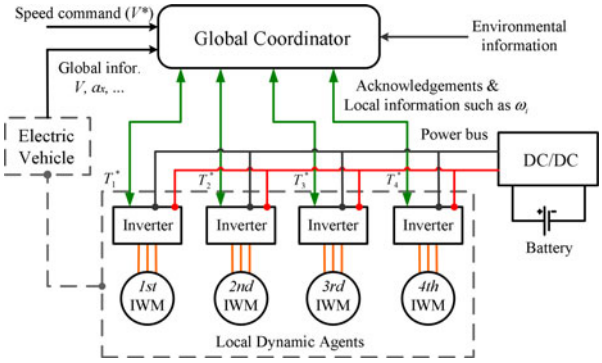

Fig. 1. Global and local structure illustration of an EV.

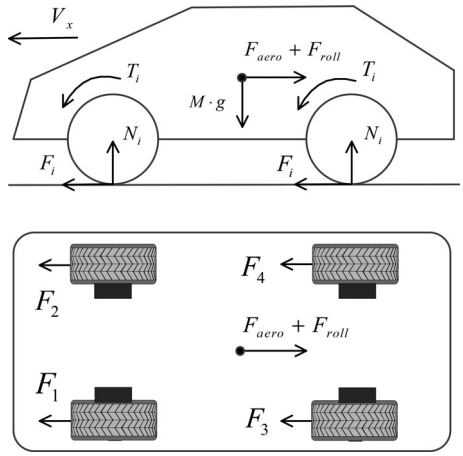

Fig. 2. Modeling of an EV with IWMs.

Section V

$$M \cdot \dot{V}_x = F_{\text{all}} - F_{\text{aero}} - F_{\text{roll}} = \sum_{i=1}^{4} F_i - \frac{1}{2} \cdot \rho_{\text{air}} \cdot C_{\text{drag}} \cdot A_{\text{front}} \cdot V_x^2 - f_R \cdot M \cdot g. \tag{1}$$

For a single wheel, the governing dynamics equation can be given as (2), and $M_{\text{roll},i}$ is generally influenced by many factors such as road condition, tire type, etc. For control design, the effects of rolling resistance moments on all wheels can be replaced by F_{roll}, which is assumed to be applied to the vehicle directly as given in (1)

$$J_i \cdot \dot{\omega}_i = T_i - F_i \cdot r - M_{\text{roll},i}. \tag{2}$$

Furthermore, an important characteristic for wheel dynamics is the slip ratio, which is given as

$$\lambda_i = \frac{V_{\omega,i} - V_x}{\max\left(V_{\omega,i}, V_x\right)} \quad \text{where } V_{\omega,i} = \omega_i \cdot r. \tag{3}$$

In (3), $V_{\omega,i}$ is greater than V_x when accelerating and is less than V_x when decelerating. Moreover, considering that the friction coefficient between the tire and the road is a function of slip ratio as shown in Fig. 3, F_i can be represented as

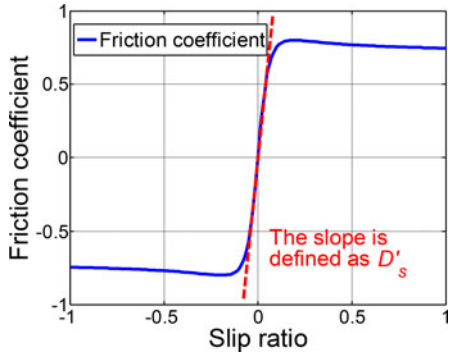

Fig. 3. Typical curve of friction coefficient and slip ratio.

$$F_i = \mu_i(\lambda_i) \cdot N_i. \tag{4}$$

In this study, λ_i is assumed to be small; therefore, μ_i can be assumed to be proportional to λ_i, and the slope in Fig. 3 is defined as D'_s (in this study, it is assumed that the four wheels are on the same kind of road, i.e., all the D'_s are identical). Then, F_i can be represented as (5) by introducing $D_{s,i}$ into (3) [30]

$$F_i = D_{s,i} \cdot \lambda_i \approx D'_s \cdot N_i \cdot \lambda_i. \tag{5}$$

To distribute torque to save energy, one of the factors that can be utilized is load transfer between the front and rear axles [22]. This load transfer is caused by acceleration and deceleration. The normal forces on the four wheels are

$$N_1 = N_2 = \frac{M \cdot \left(l_r \cdot g - h_g \cdot \dot{V}_x\right) - F_{\text{aero}} \cdot h_{\text{aero}}}{2 \cdot l} \tag{6}$$

$$N_3 = N_4 = \frac{M \cdot \left(l_f \cdot g + h_g \cdot \dot{V}_x\right) + F_{\text{aero}} \cdot h_{\text{aero}}}{2 \cdot l}. \tag{7}$$

Here, only longitudinal vehicle motion is considered, and the left and right normal forces are, therefore, the same.

B. Torque Distribution Model

The commanded torque of the driver can be distributed to the four wheels to save energy; a simple distribution model will be explained further in this section. The total driving torque of a vehicle is the sum of the driving torques of all the wheels as given in (8). Therefore, the driving torque at each wheel can be set differently to achieve a desired operation point in real time, as long as the total driving torque matches the driver's torque requirement

$$T_{\text{all}} = T_1 + T_2 + T_3 + 4. \tag{8}$$

The driving torque at each wheel is defined as (9) by ignoring inertial torques [23], where $k = 0$ means front drive only and $k = 1$ means rear drive only

$$T_i = F_i \cdot r = \begin{cases} \frac{r}{2} \cdot (1-k) \cdot F_{\text{all}}, i = 1, 2 \\ \frac{r}{2} \cdot k \cdot F_{\text{all}}, i = 3, 4. \end{cases} \tag{9}$$

Moreover, from (5) and (9), slip ratio of each wheel can be expressed as

$$\lambda_i = \begin{cases} \dfrac{(1-k)\cdot F_{\text{all}}}{2\cdot D_s'\cdot N_i}, i = 1,2 \\ \dfrac{k\cdot F_{\text{all}}}{2\cdot D_s'\cdot N_i}, i = 3,4. \end{cases} \tag{10}$$

III. Optimal Torque Distribution Law

Given that the required vehicle velocity is satisfied, the driving range of an EV can be increased by minimizing the input power to the inverters. The input power can be expressed as

$$P_{\text{in}} = P_{\text{out}} + P_{\text{iron}} + P_{\text{copper}} + P_f + P_{\text{inv}} \tag{11}$$

where P_f and P_{inv} are assumed to be uncontrollable in this study, and they are, therefore, neglected in the derivation of k_{opt}. In addition, all the four wheels are directly driven by IWMs. The total motor output P_{out} is given as

$$P_{\text{out}} = \sum_{i=1}^{4} T_i \cdot \omega_i. \tag{12}$$

Next, P_{in} will be shown to be a function of torque distribution ratio. Given a velocity pattern, an optimal distribution ratio k_{opt} can be designed to minimize P_{in}, i.e., the efficiency between the total motor output and the input power to the inverters can be optimized.

A. Motor Output Power

As can be seen from (12), motor torques and angular velocities are needed to calculate motor output power. Motor torque can be obtained by (9). Based on the definition of slip ratio, wheel angular velocity is formulated as

$$\omega_i = \begin{cases} \dfrac{V_x}{r}\cdot\dfrac{1}{1-\lambda_i}, V_x \geq V_{\omega,i} \\ \dfrac{V_x}{r}\cdot(1+\lambda_i), V_x < V_{\omega,i}. \end{cases} \tag{13}$$

By inserting (9) and (13) into (12), (14) is obtained. From (10) and (14), it is seen that P_{out} is also a function of k

$$P_{\text{out}} = \begin{cases} F_{\text{all}}\cdot V_x\cdot\left(\sum\limits_{i=1}^{2}\dfrac{1-k}{2\cdot(1-\lambda_i)}+\sum\limits_{i=3}^{4}\dfrac{k}{2\cdot(1-\lambda_i)}\right), V_x \geq V_{\omega,i} \\ F_{\text{all}}\cdot V_x\cdot\left(1+\sum\limits_{i=1}^{2}\dfrac{\lambda_i}{2}+k\cdot\left(\sum\limits_{i=3}^{4}\dfrac{\lambda_i}{2}-\sum\limits_{i=1}^{2}\dfrac{\lambda_i}{2}\right)\right), V_x < V_{\omega,i}. \end{cases} \tag{14}$$

B. Motor Losses

Copper and iron losses were formulated as a function of the torque distribution ratio. For the sake of completeness, Park transformation-based d-q equivalent circuits of a PMSM are illustrated in Fig. 4 [24]. Copper loss of the ith motor can be modeled as (15) by considering q-axis and d-axis losses

$$P_{c,i} = \frac{3}{2}R_i\cdot\left(i_{d,i}^2 + i_{q,i}^2\right). \tag{15}$$

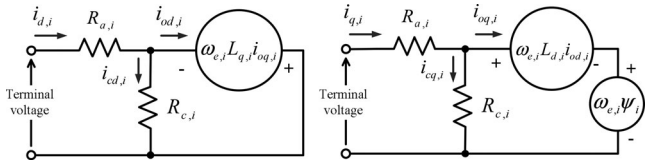

Fig. 4. Equivalent circuits of the ith PMSM.

Considering that the q-axis current $i_{q,i}$ is proportional to the torque, (15) can be alternatively represented as (16) by introducing the torque coefficient $K_{t,i}$

$$P_{c,i} = \frac{3}{2}R_{a,i}\cdot\left[i_{d,i}^2 + \left(\frac{T_i}{K_{t,i}}\right)^2\right]. \tag{16}$$

Additionally, $K_{t,i}$ can be given by the number of pole pairs $p_{n,i}$ and the interlinkage magnetic flux ψ_i as

$$K_{t,i} = p_{n,_i}\cdot\Psi_i. \tag{17}$$

To maximize output torque, the d-axis current can be controlled to be zero [25], i.e., the q-axis current is much bigger than the d-axis current. The total copper loss can then be formulated as (18).

Next, it can be known from Fig. 4 that $i_{cd,i}\cdot R_{c,i} = \omega_{e,i}\cdot L_{q,i}\cdot i_{oq,i}$ and $i_{cq,i}\cdot R_{c,i} = \omega_{e,i}\cdot L_{d,i}\cdot i_{od,i} + \omega_{e,i}\cdot\psi_i$. The iron loss of the ith

$$\begin{aligned} P_{\text{copper}} &= \sum_{i=1}^{4}\left[\frac{3}{2}\cdot R_{a,i}\cdot\left(i_{d,i}^2+\frac{T_i^2}{K_{t,i}^2}\right)\right] \\ &\approx \sum_{i=1}^{4}\left(\frac{3}{2}\cdot\frac{R_{a,i}\cdot T_i^2}{K_{t,i}^2}\right) = \sum_{i=1}^{4}\left(\frac{3}{2}\cdot\frac{R_{a,i}}{p_{n,i}^2\cdot\Psi_i^2}\cdot T_i^2\right) \\ &= \frac{3\cdot F_{\text{all}}^2\cdot r^2}{2}\cdot\left[\sum_{i=1}^{2}\left(\frac{R_{a,i}\cdot(1-k)^2}{4\cdot p_{n,i}^2\cdot\Psi_i^2}\right)\right. \\ &\quad \left.+\sum_{i=3}^{4}\left(\frac{R_{a,i}\cdot k^2}{4\cdot p_{n,i}^2\cdot\Psi_i^2}\right)\right] \end{aligned} \tag{18}$$

motor can, therefore, be expressed as

$$\begin{aligned} P_{i,_i} &= \frac{3}{2}\cdot R_{c,i}\cdot(i_{cd,i}^2 + i_{cq,i}^2) \\ &= \frac{3}{2}\cdot\frac{\omega_{e,i}^2}{R_{c,i}}\cdot[(L_{q,i}\cdot i_{\text{oq},i})^2 + (L_{d,i}\cdot i_{\text{od},i} + \psi_i)^2] \end{aligned} \tag{19}$$

where $i_{\text{od},i} = i_{d,i} - i_{cd,i}$ and $i_{\text{oq},i} = i_{q,i} - i_{cq,i}$. By neglecting the d-axis armature reaction $\omega_{e,i}\cdot L_{d,i}\cdot i_{\text{od},i}$, as it is much smaller than the magnetic electromotive force $\omega_{e,i}\psi_i$, (19) can be finalized as

$$\begin{aligned} P_{i,_i} &\approx \frac{3}{2}\cdot\frac{\omega_{e,i}^2}{R_{c,i}}\cdot[\Psi_i^2 + (L_{q,i}\cdot i_{\text{oq},i})^2] \\ &= \frac{3}{2}\cdot\frac{\omega_{e,i}^2}{R_{c,i}}\cdot\left[\Psi_i^2 + L_{q,i}^2\cdot\left(\frac{T_i}{K_{t,i}} - \frac{\omega_{e,i}\cdot\Psi_i}{R_{c,i}}\right)^2\right]. \end{aligned} \tag{20}$$

The total iron loss is then obtained as (21) by adding up the four IWMs' iron losses

$$P_{\text{iron}} = \sum_{i=1}^{4}\left\{\frac{3}{2}\cdot\frac{\omega_{e,i}^2}{R_{c,i}}\cdot\left[\Psi_i^2 + L_{q,i}^2\cdot\left(\frac{\mathrm{T}_i}{K_{t,i}} - \frac{\omega_{e,i}\cdot\Psi_i}{R_{c,i}}\right)^2\right]\right\}$$
$$= \sum_{i=1}^{2}\left\{\frac{3}{2}\cdot\frac{\omega_{e,i}^2}{R_{c,i}}\cdot\left[\Psi_i^2 + L_{q,i}^2\cdot\left(\frac{r\cdot(1-k)\cdot F_{\text{all}}}{2\cdot K_{t,i}} - \frac{\omega_{e,i}\cdot\Psi_i}{R_{c,i}}\right)^2\right]\right\} + \sum_{i=3}^{4}\left\{\frac{3}{2}\cdot\frac{\omega_{e,i}^2}{R_{c,i}}\cdot\left[\Psi_i^2 + L_{q,i}^2\cdot\left(\frac{r\cdot k\cdot F_{\text{all}}}{2\cdot K_{t,i}} - \frac{\omega_{e,i}\cdot\Psi_i}{R_{c,i}}\right)^2\right]\right\}. \quad (21)$$

The equivalent core-loss resistance is given as

$$\frac{1}{R_{c,i}} = \frac{1}{R_{c0,i}} + \frac{1}{R_{c1,i}\cdot|\omega_{e,i}|} \quad (22)$$

where $R_{c0,i}$ and $R_{c1,i}$ are the eddy current loss and hysteresis loss, respectively [26]. Furthermore, $\omega_{e,i}$ can be expressed using the vehicle speed as $\omega_{e,i} = V_x p_{n,i}/r$. Finally, from (18) and (21), both P_{copper} and P_{iron} are functions of k.

C. Optimal Torque Distribution Ratio

Substituting (14), (18), and (21) into (11), P_{in} can be formulated in two cases, both of which are quadratic functions of k. Therefore, the optimal ratio k_{opt} can be obtained by solving the partial differential equation $\partial P_{\text{in}}/\partial k|k=k_{\text{opt}} = 0$, and the optimal distribution ratio k_{opt} can be approximated as

$$k_{\text{opt}} = \frac{\frac{V_x}{2\cdot D_s'}\cdot\sum_{i=1}^{2}\frac{1}{N_i} + \frac{3\cdot r^2}{4}\cdot\sum_{i=1}^{2}\frac{R_{a,i}}{K_{t,i}^2} + \frac{3\cdot V_x^2}{4}\cdot\sum_{i=1}^{2}\frac{L_{q,i}^2}{R_{c,i}\cdot\Psi_i^2}}{\frac{V_x}{2\cdot D_s'}\cdot\left(\sum_{i=1}^{4}\frac{1}{N_i}\right) + \frac{3\cdot r^2}{4}\cdot\sum_{i=1}^{4}\frac{R_{a,i}}{K_{t,i}^2} + \frac{3\cdot V_x^2}{4}\cdot\sum_{i=1}^{4}\frac{L_{q,i}^2}{R_{c,i}\cdot\Psi_i^2}}. \quad (23)$$

IV. Controller Design and Stability Analysis

After the torque distribution law has been established, torque control of each wheel should be implemented. Moreover, as locally stable controllers cannot guarantee global stability, stability analysis of the overall control system is necessary.

A. Controller Design for RECS

From (2), the derivative of ω_i is obtained as

$$\dot{\omega}_i = \frac{1}{J_i}(T_i - F_i\cdot r_i). \quad (24)$$

For four wheels, a state-space equation can then be constructed as follows based on (9) and (24)

$$\dot{\omega} = A\cdot F + B\cdot T_{\text{all}} \quad (25)$$

where

$$\omega = [\omega_1,\omega_2,\omega_3,\omega_4]^T, F = [F_1,F_2,F_3,F_4]^T$$

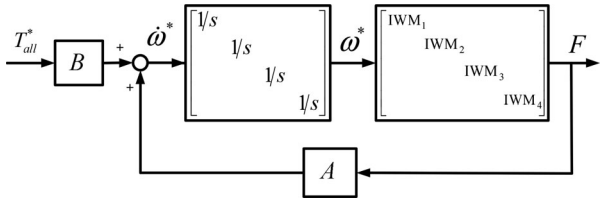

Fig. 5. Block diagram of the control system.

$$A = \text{diag}\left(\frac{-r_1}{J_1},\frac{-r_2}{J_2},\frac{-r_3}{J_3},\frac{-r_4}{J_4}\right)$$
$$B = \left[\frac{1-k}{2\cdot J_1},\frac{1-k}{2\cdot J_2},\frac{k}{2\cdot J_3},\frac{k}{2\cdot J_4}\right]^T.$$

That is, the overall control system can be constructed as Fig. 5, where the *IWM*$_i$ represents the ith local dynamic agent. It can be observed that the input to a local agent is the reference of the wheel angular velocity and the output is the driving force of the ith wheel. A detailed description of the system is illustrated in Fig. 6. Clearly, the control system has two loops: the outer loop based on (25); and the inner loop is a wheel velocity control loop. The wheel velocity is available from an encoder.

1) Driving Force Observer (DFO): As can be seen in Fig. 6, driving forces are required to construct the feedback loops. However, they are difficult to measure directly. In this research, the DFO is employed to estimate the forces [21]. Fig. 7 illustrates the principle of the DFO, in which two forces are defined: $\hat{F}_{d,i}$ is the estimated force without filtering, and $\hat{F}_i$ is the estimation after a low-pass filter (LPF). By neglecting the resistance forces, (26) can be obtained from (1), (3), and (9)

$$\hat{F}_{d,i} = \Delta_{Q,i}\cdot\omega_i\cdot s$$
$$\text{where } \Delta_{Q,i} = \begin{cases}\dfrac{r\cdot M\cdot(1-k)}{2}, i=1,2\\ \dfrac{r\cdot M\cdot k}{2}, i=3,4.\end{cases} \quad (26)$$

For four wheels, based on (26), DFOs can be rearranged as (27) by taking the LPFs into account

$$\hat{F} = \left[\hat{F}_1,\ \hat{F}_2,\ \hat{F}_3,\ \hat{F}_4\right]^T = \left[\hat{F}_{d,1},\ \hat{F}_{d,2},\ \hat{F}_{d,3},\ \hat{F}_{d,4}\right]^T\cdot\frac{1}{\tau\cdot s+1} = Q\cdot\left[\omega_1,\ \omega_2,\ \omega_3,\ \omega_4\right]^T\cdot\frac{s}{\tau\cdot s+1} \quad (27)$$

where Q is defined as diag($\Delta_{Q,1}$, $\Delta_{Q,2}$, $\Delta_{Q,3}$, $\Delta_{Q,4}$).

2) Wheel Velocity Controller (WVC): Wheel dynamics can be described as torque-input and angular-velocity-output. To derive the transfer function, first, (2) is transformed into

$$\sum_{i=1}^{4}(J_i\cdot\dot{\omega}_i) = \sum_{i=1}^{4}T_i - r\cdot\sum_{i=1}^{4}F_i. \quad (28)$$

By neglecting the resistance forces of (1) and substituting it into (28), the relationship between the input torque and the

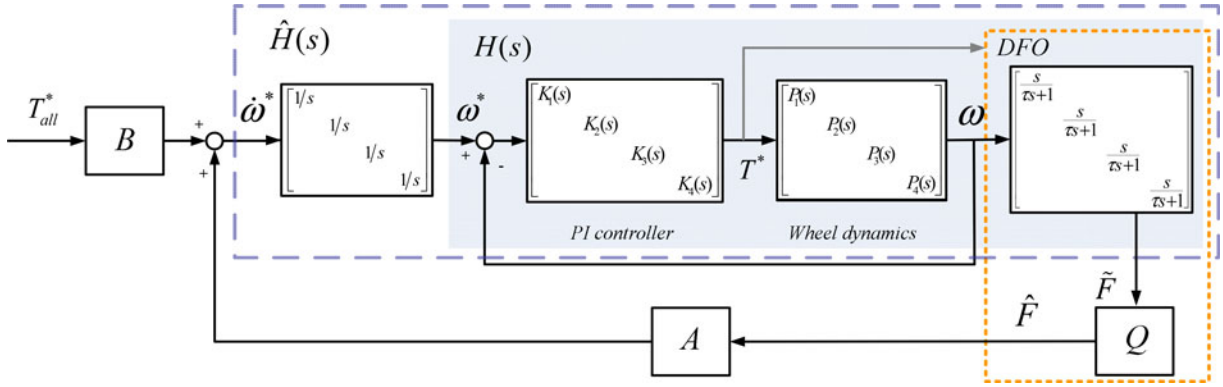

Fig. 6. Detailed representation of the overall control system.

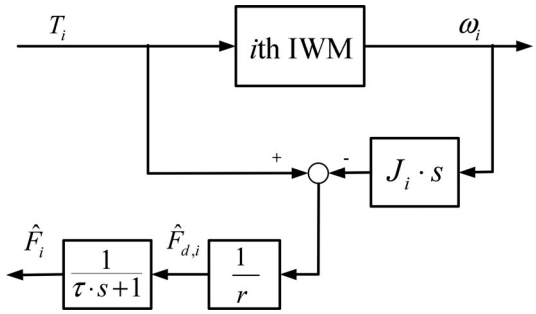

Fig. 7. Block diagram of DFO.

output wheel angular velocity can be obtained as

$$\sum_{i=1}^{4} T_i = \sum_{i=1}^{4} \left(J_i \cdot \dot{\omega}_i\right) + M \cdot r^2 \cdot \dot{\omega}_i. \tag{29}$$

For the *i*th wheel, the plant can then be nominalized as

$$P_i(s) = \frac{\omega_i}{T_i} = \frac{1}{\left(\frac{M \cdot r^2}{4} + J_i\right) \cdot s} := \frac{1}{\Delta_{G,i} \cdot s}. \tag{30}$$

Assuming the wheel velocity is controlled by a PI-controller, the inner-loop transfer function $H_i(s)$ in Fig. 6 is then derived as

$$H_i(s) = \frac{\left(K_P \cdot s + K_I\right) \cdot s}{\left(\Delta_{G,i} \cdot s^2 + K_P \cdot s + K_I\right) \cdot (\tau \cdot s + 1)} \tag{31}$$

where K_P and K_I are the proportional and integral gains. Moreover, $\hat{H}_i(s)$is defined as$H_i(s)/s$.

B. Stability Analysis

From Fig. 6, $G(s)$ from T_{all} to $\tilde{F}$ is obtained as

$$\begin{aligned} G(s) &= \left(\frac{1}{\hat{H}(s)} \cdot I_n - A \cdot Q\right)^{-1} \cdot B \\ &= \mathcal{F}_u\left(\begin{bmatrix} A \cdot Q & B \\ I_n & 0 \end{bmatrix}, \hat{H}(s) \cdot I_n\right) \end{aligned} \tag{32}$$

where $\mathcal{F}_u$ denotes the upper linear fractional transformation, and $\hat{H}(s)$ is used to represent $\hat{H}_i(s)$, as the four wheels have the same dynamics. Considering a transfer function in the form of $L(s) = (s \cdot I_n - A \cdot Q)^{-1} \cdot B$, the following equations exist

$$G(s) = L\left(\phi(s)\right), \phi(s) := 1/\hat{H}(s). \tag{33}$$

As can be observed, $G(s)$ of (34) can be generated by just replacing the s of $L(s)$ with $\phi(s)$. Therefore, the transformed transfer function $G(s)$ can be seen to have a generalized frequency variable $\phi(s)$. The domains Ω_+ and Ω_+^c in the complex plane are defined as

$$\Omega_+ := \phi(C_+), \Omega_+^c := C \backslash \Omega_+. \tag{34}$$

Then, the proposition made in [18] can be applied to the system as: $G(s) = L(\phi(s))$, which is stable if and only if all of the eigenvalues of $A \cdot Q$ are located in Ω_+^c. A detailed derivation can be found in [18]–[20]. In this application, $\phi(s)$ is obtained as

$$\begin{aligned} \phi(s) &= 1/\hat{H}(s) = \frac{(\tau \cdot s + 1) \cdot \left(\Delta_G \cdot s^2 + K_p \cdot s + K_I\right)}{K_p \cdot s + K_I} \\ &= \frac{c \cdot s^3 + d \cdot s^2 + e \cdot s + b}{a \cdot s + b}. \end{aligned} \tag{35}$$

Then, the domains Ω_+ and Ω_+^c can be characterized in the complex plane; considering that these regions are partitioned by the image of $\phi(j\omega)$, where $\omega \phi R$, the real and imaginary parts of $\phi(j\omega)$ can be defined as follows $(f(\omega) := Re[\phi(j\omega)]$ and $g(\omega) := Im[\phi(j\omega)])$:

$$f(\omega) = \frac{-a \cdot c \cdot \omega^4 + (a \cdot e - b \cdot d) \cdot \omega^2 + b^2}{a^2 \cdot \omega^2 + b^2} \tag{36}$$

$$g(\omega) = \frac{(a \cdot d - b \cdot c) \cdot \omega^3 - b \cdot (a - e) \cdot \omega}{a^2 \cdot \omega^2 + b^2}. \tag{37}$$

The intersecting points of $\phi(j\omega)$ and the imaginary axis can be calculated by finding ω_I, which satisfies $f(\omega_I) = 0$, and then, calculating $g(\omega_I)$. Similarly, the intersecting points of $\phi(j\omega)$ and the real axis can be determined from $f(\omega_R)$ where ω_R satisfies $g(\omega_R) = 0$. Here, ω_R and ω_I are given as (38) and (39), where ω_I has two roots, and ω_R has one or three roots depending on the existence of $\omega_R^{2,3}$

$$\omega_R^1 = 0, \left(\omega_R^{2,3}\right)^2 = \frac{b \cdot (a - e)}{a \cdot d - b \cdot c} \tag{38}$$

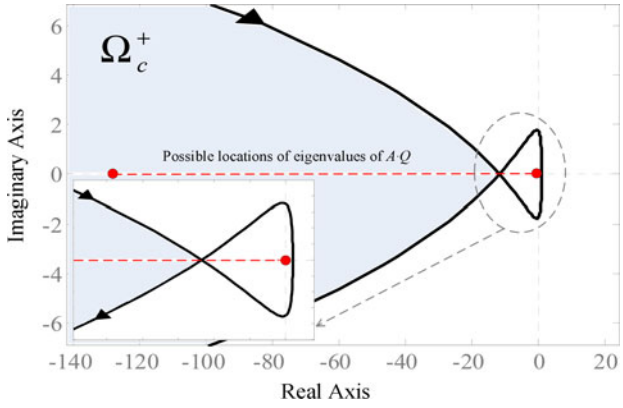

Fig. 8. Stability analysis based on eigenvalue locations (unstable case).

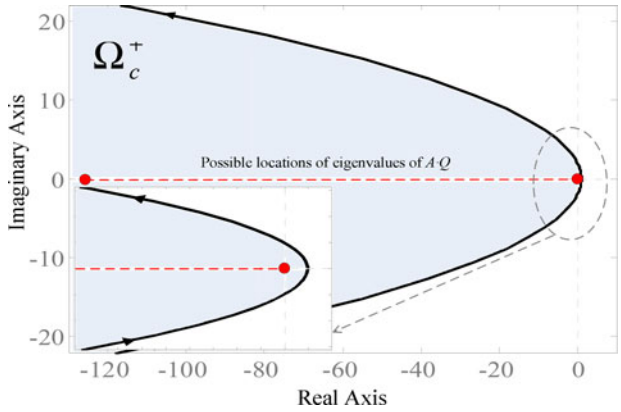

Fig. 9. Stability analysis based on eigenvalue locations (stable case).

$$\left(\omega_I^{1,2}\right)^2 = \frac{(a\cdot e - b\cdot d) + \sqrt{(a\cdot e - b\cdot d)^2 + 4\cdot a\cdot b^2\cdot c}}{2\cdot a\cdot c}. \tag{39}$$

By inserting (38) and (39) into (36) and (37), respectively, it is known that $\phi(j\omega)$ has two intersecting points with the imaginary axis. For the real axis, the number of intersecting points has two possibilities: if $\omega_R^{2,3}$ exist, the number is 3, otherwise it is 1. To give a general idea of this concept, two illustrative examples are provided. The eigenvalues of $A{\cdot}Q$ are $-M\cdot r\cdot(1-k)/2$ and $-M\cdot r\cdot k/2$, where $k\ \phi\ [0, 1]$, and they range from –128.95 to 0 based on the parameters given in the Appendix.

Example 1: The poles of the local system (WVC loop) are placed at $-2.15 \pm 10.5i$, i.e., the local system can be stabilized. However, as can be seen from Fig. 8, the eigenvalues of $A{\cdot}Q$ are not in the scope of Ω_+^c; therefore, the overall system is unstable.

Example 2: The poles of the local system are placed at ± 10, i.e., the local system can be stabilized. The eigenvalues of $A{\cdot}Q$ are in the domain of Ω_+^c as can be observed in Fig. 9, which means the global system is stable.

Then, the control system is simulated using the poles of the two examples as shown in Fig. 10: the gray solid line represents the vehicle speed of example 1, which is not stable; and the red dashed line is the speed in example 2, which matches very well with the reference. These results match with the aforementioned stability analysis.

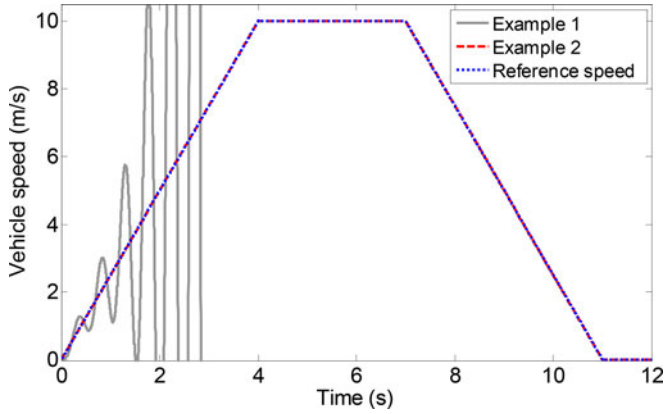

Fig. 10. Control performance comparison between the two examples.

V. Simulations and Experiments

A. Trapezoid Speed Pattern Test

To evaluate the proposed RECS, simulations and experiments were conducted to verify the proposed method. Considering that normal driving cycles are groups of several acceleration-constant speed-deceleration patterns, a speed pattern for evaluation was designed as shown in Fig. 11(a): the vehicle first accelerates at 0.25 g for 4 s, and then, cruises for 3 s at a constant speed of 10 m/s, finally decelerating at –0.25 g until stopping. For comparison, energy consumption based on different distribution ratios were also studied ($k = 1$ could not be realized due to the limited power of the rear motors), and these ratios are shown in Fig. 11(b); obviously, $k_{\rm opt}$ changes with time, while the others are constant. Specifically, as the mean value of $k_{\rm opt}$ for the trapezoid speed pattern is about 0.28, $k = 0.28$ was also considered.

To better represent the vehicle plant in the simulations, the Magic Formula was employed to describe the tire dynamics [29]. Furthermore, as part of the vehicle plant, aerodynamic drag and rolling resistance were included for vehicle speed calculation. The vehicle was assumed to run on a high friction road, and the slope of $\mu - \lambda$ curve $D^{'}{}_s$, the rolling coefficient f_R, and the air density $\rho_{\rm air}$ were set to 10, 0.00836, and 1.215 kg/m^3, respectively. Moreover, the consumed energy was calculated as (40) by integrating $P_{\rm in}$ in (11). Specifically, the friction loss was considered in the calculation of $P_{\rm in}$ and was modeled to be proportional to the motor speed, and the loss of inverters is modeled as 5% of $P_{\rm in}$, i.e., the efficiency of the inverters was assumed to be 95%

$$E_{\rm in} = \int P_{\rm in}{\rm d}t. \tag{40}$$

In the experiments, our original experimental EV was utilized, and its parameters are provided in the Appendix. The energy consumptions were obtained by measuring the input power to the inverters, and the evaluation equation is represented as

$$E_{\rm in} = V_{\rm dc}\cdot I_{\rm dc} = V_{\rm dc}\cdot\sum_{i=1}^{4} I_{{\rm dc},i} \tag{41}$$

where $V_{\rm dc}$ is the dc-bus voltage, which is measured by an on-board Yokogawa differential probe, $I_{{\rm dc},i}$ and $I_{\rm dc}$ are the input

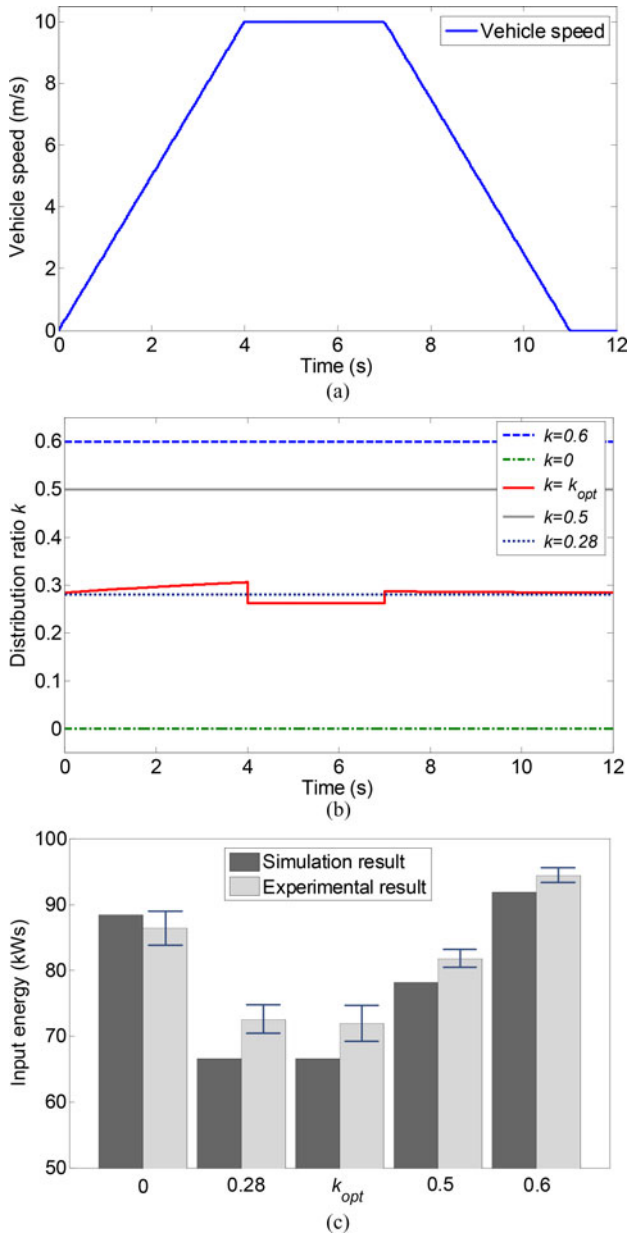

Fig. 11. Simulation and experimental results under different distribution ratios. (a) Vehicle speed pattern. (b) Torque distribution ratio comparison. (c) Input energy comparison of different *k*.

current to the *i*th inverter and the sum of $I_{\mathrm{dc},i}$, respectively. $I_{\mathrm{dc},i}$ was measured by an onboard Tektronix current probe. As mentioned earlier, experiments based on different torque distribution ratios were conducted, and each case was conducted three times to remove the uncertainties during each experiment.

The comparison of the required energy for both simulations and experiments are shown in Fig. 11(c): each dark gray bar shows energy consumption for a specific distribution ratio in the simulation; each light gray bar gives average value of the experimental results for a particular distribution ratio; and the error bar on top represents the range of the three experimental values. As can be seen, the cases when k equals k_{opt} and 0.28 show lower energy consumption when compared with the other cases. Although differences exist between simulated and experimental results that may had been caused by modeling errors and unconsidered items, the tendencies matched very well. To clearly see the energy consumption difference among k_{opt}, 0.28, and other ratios, these cases are represented in terms of cruising range per kilowatt-hour as given in Table I based on (42), and the proposed torque management method can drive the EV longer than other distribution ratios

TABLE I
CRUISING RANGE COMPARISON (UNITS: KM)

Distribution Ratio	0	0.28	0.5	0.6	k_{opt}
Cruising range per kilowatt-hour (sim.)	2.85	3.78	3.2	2.74	3.79
Cruising range per kilowatt-hour (exp.)	2.92	3.47	3.08	2.67	3.5

$$\text{Cruising range per kilowatt-hour} = \frac{3600 \cdot l_d}{E_{\mathrm{in}}}. \quad (42)$$

B. New European Driving Cycle (NEDC) Test

To better address real driving conditions, the NEDC test was employed to evaluate the proposed control system. As mentioned previously, the IWMs' power of our experimental EV is limited. Therefore, only a simulation was conducted using NEDC test, and the NEDC profile is shown in Fig. 12(a). Clearly, the NEDC consists of many trapezoid speed patterns like the one discussed previously. The optimal k for the NEDC is given in Fig. 12(b), and it varies depending on vehicle speed. As the mean value of k_{opt} was about 0.3, it was selected together with 0, 0.5, and 0.6 for the comparison with the k_{opt} case. The values of input energy are shown in Fig. 12(c), which illustrates that the input energy in the case of k_{opt} is smallest among all of the energy consumptions.

From the trapezoid speed pattern and NEDC tests, it can be seen that the optimal torque distribution ratios vary at around 0.3, and for a given EV, it is, therefore, acceptable to use a static approximate-optimal ratio. However, as can be known from (23), k not only has relationship with vehicle speed, but also relates with motor parameters. For example, overheating of the motor can cause the increase of armature winding resistance and the decrease of q-axis inductance. Thus, online motor parameter estimation [31] and adaption of the distribution ratio has to be addressed in such cases.

VI. CONCLUSION AND FUTURE WORKS

In this paper, a pure control methodology, torque distribution-based RECS, was proposed to increase the cruising range of four wheel independent driven EVs. The torque distribution law was determined by the weight transfer between the front and rear axles and motor losses. Considering the specific structure, an EV with four IWMs was considered as an LTI system with four generalized frequency variables. That is, based on the torque commands from the main controller, the four wheels can be independently controlled by local controllers. For such a global-local system, a stability criterion was employed for the design of the controller, and the stability criterion is also applicable to the mechatronic system with multiple homogeneous actuators [19]. Because vehicles and motors are complex mechatronic systems with uncertainties, one of the possible

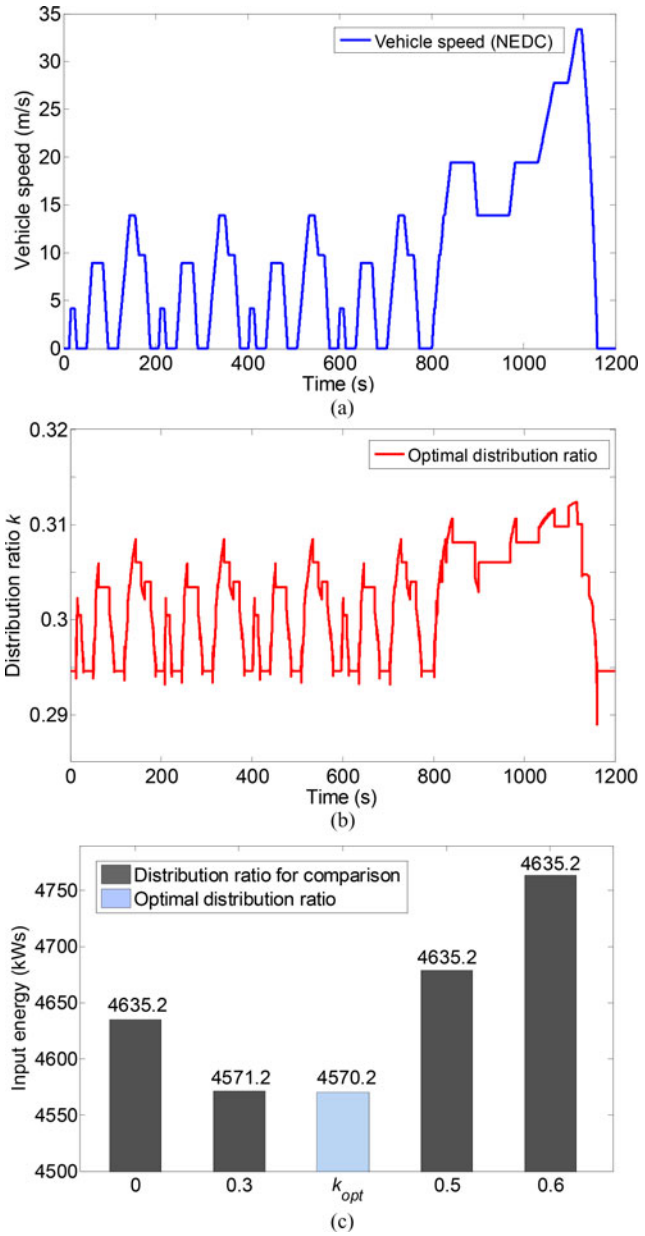

Fig. 12. Simulation results under NEDC test. (a) Speed pattern of NEDC. (b) Optimal torque distribution ratio for NEDC. (c) Input energy comparison of different *k*.

future works of this study is to further develop the control system with frequency control [28] or uncertainty management strategies [27]. In the modeling of copper loss, *d*-axis current is assumed to be zero; however, for high-speed applications, *d*-axis current has to be considered as it is used for field weakening.

APPENDIX

The experimental EV used in this research has four IWMs that can be independently controlled, and the IWMs and their controllers were provided by Toyo Denki. The vehicle controller is a dSPACE AUTOBOX-DS1103, and the algorithm in this research was implemented and evaluated in a model-based design manner. In Fig. A1, photos of the EV, the vehicle controller, an inverter, and an IWM are shown, and in Table AI, the vehicle/IWM parameters related with this research are provided. It should be noted that: 1) the prototype IWMs were provided by Toyo Denki, however, the selection of motor parameters can be considered for further reduction of energy consumption and 2) the wheel inertias and motor parameters of the front and rear wheels are slightly different, but the proposed method is also applicable to normal EVs with four identical wheels/IWMs.

Fig. A1. Experimental EV, Dspace controller, inverter, and IWM.

TABLE AI
SPECIFICATIONS OF EXPERIMENTAL SETUP

Symbol	Description	Value
Vehicle Parameters		
M	vehicle mass	850 kg
h_g	Height of center of gravity (CoG)	0.51 m
l_f	distance from CoG to front axle	1.013 m
l_r	distance from CoG to rear axle	0.702 m
J_i	spin inertial of the *i*th wheel	1.24 kg·m^2 ($i=1,2$)/ 1.26 kg·m^2 ($i=3,4$)
r	wheel radius	0.301 m
C_{drag}	aerodynamic drag coefficient	0.48
A_{front}	vehicle front area	2.4 m^2
Parameters of the *i*th IWM		
$R_{a,i}$	armature winding resistance	0.086 Ω ($i=1,2$)/ 0.143 Ω ($i=3,4$)
$R_{c0,i}$	eddy current loss	300 Ω ($i=1,2,3,4$)
$R_{c1,i}$	hysteresis loss	0.13 Ω ($i=1,2$)/ 0.0525 Ω ($i=3,4$)
ψ_i	inter-linkage magnetic flux	0.18 Wb ($i=1,2$)/ 0.125 Wb ($i=3,4$)
$p_{n,i}$	number of pole pair	10 ($i=1,2$)/ 12 ($i=3,4$)
$L_{q,i}$	*q*-axis inductance	0.00069 H ($i=1,2$)/ 0.0015 H ($i=3,4$)
$L_{d,i}$	*d*-axis inductance	0.00063 H ($i=1,2$)/ 0.0013 H ($i=3,4$)

REFERENCES

[1] Y. Hori, "application of electric motor, supercapacitor, and wireless power transfer to enhance operation of future vehicles," in *Proc. IEEE Int. Symp. Ind. Electron.*, Jul. 2010, pp. 3633–3635.
[2] Z. Liu, F. Wen and G. Ledwich, "Optimal planning of electric-vehicle charging stations in distribution systems," *IEEE Trans. Power Del.*, vol. 28, no. 1, pp. 102–110, Jan. 2013.
[3] C. S. S. Sarma, "Energy harvesting and intelligent load sharing for electric hybrid vehicles: A system perspective," in *Proc. Annu. IEEE India Conf.*, 2011, pp. 1–5.
[4] K. T. Chau, C. C. Chan, and C. Liu, "Overview of permanent-magnet brushless drives for electric and hybrid electric vehicles," *IEEE Trans. Ind. Electron.*, vol. 55, no. 6, pp. 2246–2257, Jun. 2008.
[5] H. Liu, X. Chen and X. Wang, "Overview and prospects on distributed drive electric vehicles and its energy saving strategy," *Przegląd Elektrotechniczny (Electrical Review)*, vol. 88, no. 7a, pp. 122–125, 2012.

[6] H. Fujimoto and H. Sumiya, "Advanced safety range extension control system for electric vehicle with front- and rear-active steering and left- and right-force distribution," in *Proc. IEEE/ASME Int. Conf. Advanced Intell. Mechatronics*, 2012, pp. 532–537.
[7] X. Yuan and J. Wang, "Torque distribution strategy for a front-and rear-wheel-driven electric vehicle," *IEEE Trans. Veh. Technol.*, vol. 61, no. 8, pp. 3365–3374, Oct. 2012.
[8] Y. P. Yang, Y. C. Shih and J. M. Chen, "Real-time driving strategy for a pure electric vehicle with multiple traction motors by particle swarm optimization," in *Proc. 7th IET Int. Conf. Power Electron., Mach. Drives*, 2014, pp. 1–6.
[9] N. Mutoh, "Driving and braking torque distribution methods for front- and rear-wheel-independent drive-type electric vehicles on roads with low friction coefficient," *IEEE Trans. Ind. Electron.*, vol. 59, no. 10, pp. 3919–3933, Oct. 2012.
[10] Y. Chen and J. Wang, "Design and experimental evaluations on energy efficient control allocation methods for overactuated electric vehicles: Longitudinal motion case," *IEEE Trans. Mechatronics*, vol. 19, no. 2, pp. 538–548, Apr. 2014.
[11] R. Wang, Y. Chen, D. Feng, X. Huang, and J. Wang, "Development and performance characterization of an electric ground vehicle with independently actuated in-wheel motors," *J. Power Sources*, vol. 196, no. 8, pp. 3962–3971, 2011.
[12] N. Mutoh, T. Kato and K. Murakami, "Front and rear wheel independent drive type electric vehicle (FRID EV) taking the lead for next generation eco-vehicles," *SAE Paper, 2011–39–7206*, 2011.
[13] Y. Hori, "Future vehicle driven by electricity and control-research on four wheel motored UOT electric March II," *IEEE Trans. Ind. Electron.*, vol. 51, no. 5, pp. 954–962, Oct. 2004.
[14] D. Li, X. Shen and F. Yu, "Integrated vehicle chassis control with main/servo-loop structure," *Int. J. Automotive Technol.*, no. 7, pp. 803–812, vol. 7, no. 7, 2006.
[15] B. C. Chen and C. C. Kuo, "Electronic stability control for electric vehicle with four in-wheel motors," *Int. J. Automotive Technol.*, vol. 15, no. 4, pp. 573–580, Jun. 2014.
[16] A. Stern, Z. Shiller, "Control allocation of all-wheel drive vehicles: A longitudinal model," in *Proc. IEEE/RSJ Int. Conf. Intell. Robots Syst.*, 2013, pp. 2862–2867.
[17] C. Vermillion, J. Sun, and K. Butts, "Model predictive control allocation for overactuated systems— Stability and performance," in *Proc. 46th IEEE Conf. Decision Control*, 2007, pp.1251–1256.
[18] S. Hara, T. Hayakawa, and H. Sugata, "LTI Systems with generalized frequency variables: A unified framework for homogeneous multi-agent dynamical systems," *SICE J. Control, Measurement, Syst. Integration*, vol. 2, no. 5, pp. 299–306, 2009.
[19] S. Hara, H. Tanaka, and T. Iwasaki, "Stability analysis of systems with generalized frequency variables," *IEEE Trans. Autom. Control*, vol. 59, no. 2, pp. 313–326, Feb. 2014.
[20] H. Tanaka, S. Hara, and T. Iwasaki, "LMI stability condition for linear systems with generalized frequency variables," in *Proc. 7th Asian Control Conf.*, 2009, pp. 136–141.
[21] J. Amada and H. Fujimoto, "Torque based direct driving force control method with driving stiffness estimation for electric vehicle with in-wheel motor," in *Proc. 38th IEEE-IECON*, 2012, pp. 4904–4909.
[22] Y. Wang, H. Fujimoto and S. Hara, "Range extension control system for electric vehicles by LTI modeling with generalized frequency variable," in *Proc. Amer. Control Conf.*, 2014, pp. 3838–3843.
[23] T. Kanou and H. Fujimoto, "Slip-ratio based yaw-rate control with driving stiffness identification for electric vehicle," in *Proc. 9th Int. Symp. Advanced Vehicle Control*, 2008, pp. 786–791.
[24] S. Morimoto, Y. Tong, Y. Takeda and T. Hirasa, "Loss minimization control of permanent magnet synchronous motor drives," *IEEE Trans. Ind. Electron.*, vol. 41, no. 5, pp. 511–517, Oct. 1994.
[25] Y. Luo, Y. Chen and Y. Pi, "Cogging effect minimization in PMSM position servo system using dual-high-order periodic adaptive learning compensation," *ISA Trans.*, vol. 49, no. 4, pp. 479–488, 2010.
[26] S. Shinnaka, "Proposition of new mathematical models with core loss factor for controlling AC motors," in *Proc. 24th IEEE-IECON*, 1998, pp. 297–302.
[27] W. Sun, H. Gao and O. Kaynak, "Adaptive backstepping control for active suspension systems with hard constraints," *IEEE Trans. Mechatronics*, vol. 18, no. 3, pp. 1072–1079, Jun. 2013.
[28] W. Sun, H. Gao and O. Kaynak. "Finite frequency H∞ control for vehicle active suspension systems," *IEEE Trans. Control Syst. Technol.*, vol. 19, no. 2, pp. 416–422, Apr. 2011.
[29] D. Yin, S. Oh, and Y. Hori, "A novel traction control for EV based on maximum transmissible torque estimation," *IEEE Trans. Ind. Electron.*, vol. 56, no. 6, pp. 2086–2094, Jun. 2009.
[30] K. Maeda, H. Fujimoto and Y. Hori, "Four-wheel driving-force distribution. Method for instantaneous or split slippery roads for electric vehicle," *Automatika*, vol. 54, no. 1, pp. 103–113, 2013.
[31] S. J. Underwood and I. Husain, "Online parameter estimation and adaptive control of permanent-magnet synchronous machines," *IEEE Trans. Ind. Electron.*, vol. 57, no. 7, pp. 2435–2443, Jul. 2010.

Yafei Wang received the B.S. degree in internal combustion engine from Jilin University, Changchun, China, in 2005, the M.S. degree in vehicle engineering from Shanghai Jiao Tong University, Shanghai, China, in 2008, and the Ph.D. degree in electrical engineering from the University of Tokyo, Tokyo, Japan, in 2013.

From 2008 to 2010, he worked in automotive industry for nearly two years, including internship with FIAT Powertrain Technologies, and full-time working experience with Delphi China Technical Center. He is currently working as a Postdoctoral Researcher in the University of Tokyo. His research interests include state estimation and control for electric vehicles.

Hiroshi Fujimoto (S'99–M'01–SM'12) received the Ph.D. degree from the Department of Electrical Engineering, The University of Tokyo, Chiba, Japan, in 2001.

In 2001, he joined the Department of Electrical Engineering, Nagaoka University of Technology, Niigata, Japan, as a Research Associate. From 2002 to 2003, he was a Visiting Scholar with the School of Mechanical Engineering, Purdue University, West Lafayette, IN, USA. In 2004, he joined the Department of Electrical and Computer Engineering, Yokohama National University, Yokohama, Japan, as a Lecturer and went on to become an Associate Professor in 2005. Since 2010, he has been an Associate Professor with The University of Tokyo, Chiba. His interests include control engineering, motion control, nanoscale servo systems, electric vehicle control, and motor drives.

Dr. Fujimoto received the Best Paper Award from the IEEE TRANSACTIONS ON INDUSTRIAL ELECTRONICS in 2001 and 2013, the Isao Takahashi Power Electronics Award in 2010, and the Best Author Prize of the Society of Instrument and Control Engineers (SICE) in 2010. He is a member of the SICE, the Robotics Society of Japan, and the Society of Automotive Engineers of Japan, and a Senior Member of the Institute of Electrical Engineers of Japan.

Shinji Hara (M'86–SM'04–F'06) received the B.S., M.S., and Ph.D. degrees in engineering from the Tokyo Institute of Technology, Tokyo, Japan, in 1974, 1976 and 1981, respectively.

In 1984, he joined the Tokyo Institute of Technology as an Associate Professor and had served as a Full Professor for ten years. Since 2002, he has been a Full Professor in the Department of Information Physics and Computing, The University of Tokyo. His current research interests include robust control, decentralized control for networked dynamical systems, glocal control, systems biology, and computational aspects of control system design.

Dr. Hara received the George S. Axelby Outstanding Paper Award from IEEE Control System Society in 2006. He also received Best Paper Awards from the Society of Instrument and Control Engineers (SICE) several times. He was the General Chair of the CCA04, the Program Cochair of the 17th International Federation of Automatic Control (IFAC) World Congress in Seoul, the President of SICE in 2009, the Vice President of IEEE CSS for membership activities in 2009–2010, IFAC Council member since 2011, and an Associate Editors of several international journals including IEEE TRANSACTIONS ON AUTOMATIC CONTROL AND AUTOMATICA. He is a Fellow of IFAC and SICE.